The Meteoritical Society

Meteoritics & Planetary Science 52, Nr 5, 827–841 (2017)
doi: 10.1111/maps.12837

KREEP basalt petrogenesis: Insights from 15434,181

Karl CRONBERGER* and Clive R. NEAL

Department of Civil & Environmental Engineering and Earth Sciences, University of Notre Dame, Notre Dame, IN 46556, USA
*Corresponding author. E-mail: kcronber@nd.edu

(*Received 03 September 2015; revision accepted 14 December 2016*)

Abstract–Returned lunar KREEP basalts originated through impact processes or endogenous melting of the lunar interior. Various methods have been used to distinguish between these two origins, with varying degrees of success. Apollo 15 KREEP basalts are generally considered to be endogenous melts of the lunar interior. For example, sample 15434,181 is reported to have formed by a two-stage cooling process, with large orthopyroxene (Opx) phenocrysts forming first and eventually cocrystalizing with smaller plagioclase crystals. However, major and trace element analyses of Opx and plagioclase coupled with calculated equilibrium liquids are inconsistent with the large orthopyroxenes being a phenocryst phase. Equilibrium liquid rare earth element (REE) profiles are enriched relative to the whole rock (WR) composition, inconsistent with Opx being an early crystallizing phase, and these are distinct from the plagioclase REE equilibrium liquids. Fractional crystallization modeling using the Opx equilibrium liquids as a parental composition cannot reproduce the WR values even with crystallization of late-stage phosphates and zircon. This work concludes that instead of being a phenocryst phase, the large Opx crystals are actually xenocrysts that were subsequently affected by pyroxene overgrowths that formed intergrowths with cocrystallizing plagioclase.

INTRODUCTION

Meyer and Hubbard (1970) identified a component of Apollo 12 soil samples that was enriched in incompatible trace elements, specifically potassium (K), rare earth elements (REE), and phosphorus (P). This component was first termed "KREEP" by Meyer et al. (1971). The origin of KREEP as the last product from the lunar magma ocean (LMO) was explored by Warren and Wasson (1977, 1978, 1979) and Warren (1985), who termed the primordial LMO product "urKREEP."

KREEP basalts that contain derivatives of urKREEP were returned by the Apollo 14, 15, and 17 missions. They are distinguished from the more prevalent mare basalts by the abundance of Al_2O_3 (14–20 wt%; Warren 1988) and the low ratio of Ca to Al (average Ca/Al of mare basalts = 1.86 ± 0.31; KREEP basalts = 1.16 ± 0.16), which reflects the paucity of Ca-rich pyroxenes in these rock types. Two petrogeneitc models have been proposed (1) KREEP basalts are endogenous (pristine) primary magmas of the lunar interior (e.g., Dowty et al. 1976; Irving 1977; Warren et al. 1978; Ryder 1987, 1988) and (2) KREEP basalts are the result of impacts that homogenize different lithologies, including KREEP components (e.g., Irving 1975; Ryder and Bower 1976; McKay et al. 1978, 1979). Various methods have been proposed to distinguish between impact and endogenous hypotheses (e.g., Ryder 1987; Warren 1993). More recently, Neal et al. (2015) proposed a petrographic method to differentiate between endogenous basalts and impact melts by using plagioclase and olivine crystal size distributions (CSDs; see Marsh 1988, 1996, 1998, 2013). It is evident that many of the KREEP basalts returned by the Apollo 14 mission are impact melts and those from Apollo 15 and 17 are predominantly endogenous (pristine) melts of the lunar interior (e.g., Salpas et al. 1987; Taylor et al. 2012; Cronberger and Neal 2013, 2014a, 2014b; Neal et al. 2015).

Apollo 15 KREEP Basalts

Taylor et al. (2012) examined 27 Apollo 15 KREEP basalt fragments, both those local and exotic (rock

© The Meteoritical Society, 2017.

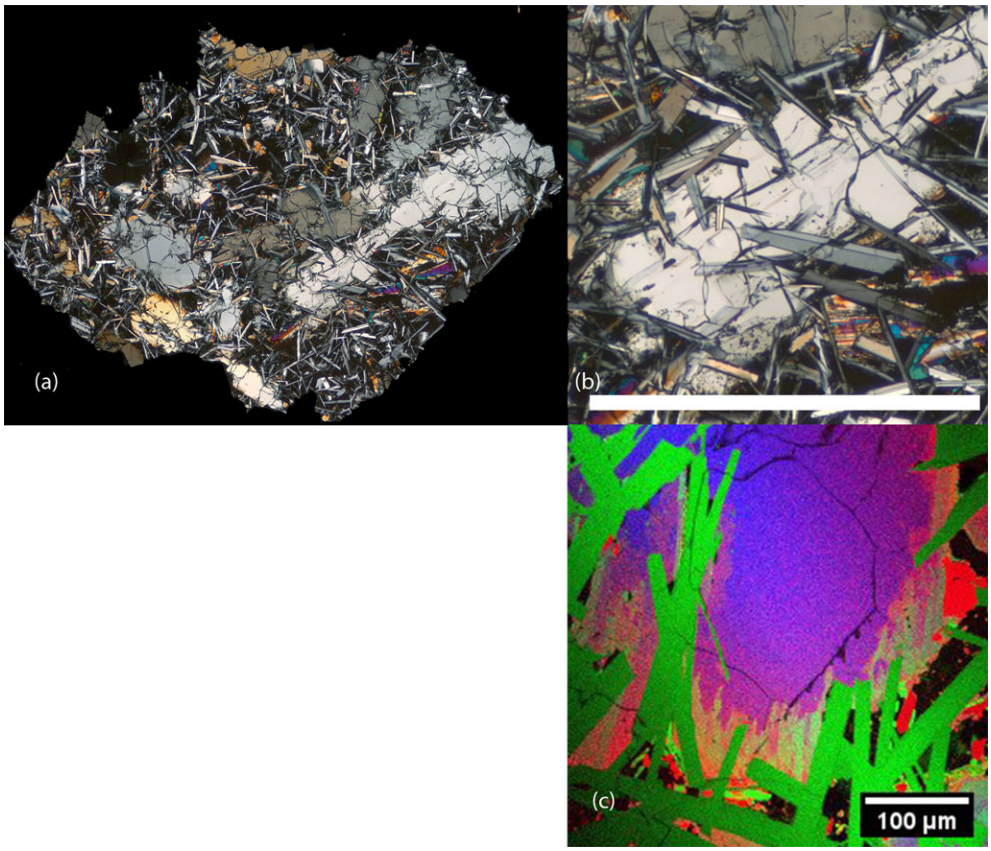

Fig. 1. a) Photomosaic of 15434,181 in XP light. The image is 5 mm across. b) Close-up of 15434,181. Plagioclase crystals are intergrown with the large Opx crystals. Scale bar is 1 mm. c) Element map of a pyroxene and intergrown plagioclase within 15434,181, Fe = Red, Ca = Green, Mg = Blue. (Color figure can be viewed at wileyonlinelibrary.com.)

fragments transported to the area by impact processes, including the parent sample of 15434,181 and 188, which is 15434,8; Lunar Receiving Laboratory 1971; Ryder and Sherman 1989) to the Hadley–Apennine area. Basalts from a common source should display an inverse relationship between Mg# (in pyroxene) versus Albite (Ab) content (in accompanying plagioclase), as demonstrated by Apollo 15 KREEP basalts (Taylor et al. 2012). Therefore, the variation of Ab in the most calcic plagioclases when plotted against the Mg# (molar Mg/[Mg + Fe] in %) in the most magnesian pyroxenes should not widely vary for basalts from a common source. Taylor et al. (2012) showed that such a plot for the Apollo 15 KREEP basalts does exhibit considerable variation, thus indicating derivation from multiple source regions. Taylor et al. (2012) also noted that many of the larger Opx crystals have core Mg# of 85–77, requiring a parent magma with an Mg# of 79–90. The Mg-rich nature of the Apollo 15 KREEP basalt parent magma would require the source region to have been dominated by phases that crystallized early from the LMO (Snyder et al. 1992; Elkins-Tanton et al. 2011; Taylor et al. 2012). To form Apollo 15 KREEP basalts, either a cumulate overturn event would be needed to mix the early- and late-stage cumulates (cf. Spera 1992; Elkins-Tanton et al. 2011) to form a hybrid source low in ilmenite that underwent partial melting, forming the KREEP basalt and Mg-Suite parent magmas (e.g., Elardo et al. 2011). Alternatively, the KREEP component could have been assimilated after the initial high-Mg parent magma was generated by the melting of a source dominated by early LMO cumulates.

Apollo 15 KREEP Basalt 15434

15434,181 was collected as part of the 4–10 mm regolith rake sample from Spur crater (Station 7) (Lunar Receiving Laboratory 1971; Ryder and Sherman 1989). Plagioclase laths (>0.25 mm) penetrate the large (up to 2 mm) Opx crystals (Fig. 1a, 1b) and this relationship was taken as evidence for the parental magma being multiply saturated (Ryder 1987; Simon et al. 1988). Resorption features are present, predominantly on the interface between the Opx and some of the larger plagioclase laths. Pigeonite-to-augite overgrowths are present on some of the large Opx

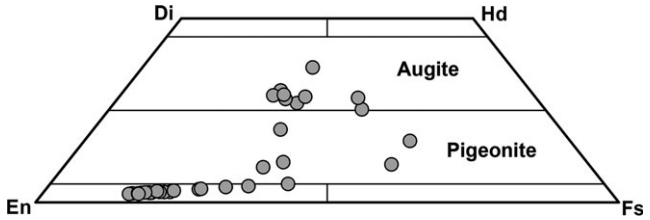

Fig. 2. Pyroxene compositions analyzed by electron probe micro analysis from thin section 15434,181.

crystals (Figs. 1c and 2). Ryder (1987) considered these overgrowths to have formed because of a change in conditions between the formation of the Opx phenocrysts and the groundmass (two-stage cooling). The whole rock (WR) composition of 15434,181 exhibits a typical LREE-enriched "KREEPy" REE profile ($[La/Yb]_N = 35.3$) with a deep negative Eu anomaly (Simon et al. 1988). Using mineral and bulk chemistry, along with petrographic evidence, Simon et al. (1988) also concluded that Apollo 15 KREEP basalts have an endogenous volcanic origin.

In this paper, we examine the origin of Apollo 15 KREEP basalt 15434,8 (the thin section from the WR sample 181 as reported by Simon et al. 1988; Fig. 1a) and its constituent mineral phases to test the two-stage cooling hypothesis of an endogenous melt of the lunar interior (Ryder 1987). In situ analyses of individual crystal phases are used to examine geochemical variations in Opx and plagioclase crystals. This approach allows the evolution of the magma to be tracked as crystallization progressed. In addition, calculated equilibrium liquids from the Opx crystals are used to evaluate a phenocryst (two-stage cooling) versus antecryst/xenocryst (two-stage cooling not required) origin for this phase and also track the evolution of the potentially unrelated parent magma.

METHODS

Using electron probe micro analysis (EPMA), we analyzed 15434,181 at Washington University in St. Louis using a JEOL JXA-8200, Toyko Japan microprobe. For analyses, acceleration voltage was 15 kV, beam current was 25 nA, and spot size was 5 μm (spot size was chosen to minimize Na evaporation in plagioclase while still small enough to get close to the rim of crystals). Elements and standards analyzed were Na (Amelia Albite P-103), Mg (Shankland syn-Forsterite P-658), Al (Alaska Anorthite NMNH 137041), Si, Ca (Gates Wollastonite), K (Madagascar Orthoclase GRR78), Mn (Mn Olivine RDS P-1087), Fe (Fe_2O_3 Elba Hematite P-238), Ti (TiO_2 GRR), and Cr (Cr_2O_3 P-585). Count time and background was 30 and 10 s, respectively, for all elements. Sodium was analyzed first to minimize the effect of evaporation during analysis of plagioclase. EPMA sites were chosen on the basis of minimal inclusion of other material (avoiding inclusions, zone changes, cracks, etc.). A total of 85 sites were analyzed, 35 in pyroxene (Table 1), and 50 in plagioclase (Table 2). Where possible, core and rim analyses were obtained.

Laser ablation inductively coupled plasma–mass spectrometry (LA-ICP-MS) analyses were conducted at the Midwest Isotope and Trace Element Research Analytical Facility (MITERAC) at the University of Notre Dame. Samples were analyzed using a Thermo Scientific (now Thermo Fisher) Element 2 high-resolution magnetic sector ICP-MS in conjunction with a New Wave UP213 laser system at a frequency of 5 Hz; a spot size of 30 μm; and where possible, a linear raster of 60 μm (dependent on crystal size). Each analysis was 3 min in length with the first minute for counting the background signal, the second was for sample analysis, and each run was followed by at least 1 min of washout time. The external standard used was the NIST 612 glass (Pearce et al. 1997). Calcium was used as an internal standard for the LA-ICP-MS analyses as determined by EPMA.

Using the method of Yao et al. (2012) and Sun and Liang (2013, and references contained therein), we calculated trace element partition coefficients for Opx. This method allows the partition coefficients for the REEs, Y, Zr, Hf, and Ti to be calculated on the basis of the mineral's major element composition. Briefly, partition coefficients are calculated in three steps (1) conversion of elemental weight % (from EPMA data) to site composition; (2) calculation of Young's modulus (E), strain-free substitution partition coefficient (D_0), and the strain-free substitution atomic radii (r_0); and (3) calculation of the partition coefficient for a given element "I" (D_i). Step 1 is accomplished by assigning the formula value of each major element to one of the sites. Step 2 utilizes equations 1, 2, and 3 in Sun and Liang (2013). R is the ideal gas constant, T is temperature in Kelvin, a_n = fitting parameters that were calculated by Yao et al. (2012) and Sun and Liang (2013), where X_i^j is the concentration of element "I" in site "J" of the pyroxene.

$$\ln D_0 = a_0 + \frac{a_1}{RT} + a_2 X_{\mathrm{Ca}}^{\mathrm{M2}} + a_3 X_{\mathrm{Al}}^{T} \quad (1)$$

$$r_0 = a_4 + a_5 X_{\mathrm{Ca}}^{\mathrm{M2}} + a_6 X_{\mathrm{Mg}}^{\mathrm{M2}} \quad (2)$$

$$E = a_7 + a_8 r_0 + a_9 X_{\mathrm{Ca}}^{\mathrm{M2}} \quad (3)$$

Step 3 then uses the lattice strain model (Blundy and Wood 1994; Wood and Blundy 2001; Equation 4 to

Table 1. Pyroxene major and minor element compositions by electron probe micro analysis (wt% oxide).

	SiO_2	TiO_2	Al_2O_3	Cr_2O_3	FeO	MnO	MgO	CaO	Na_2O	K_2O	Total
PYX 1	53.35	0.76	1.95	0.91	16.67	0.26	24.86	1.78	0.02	n.d.	100.58
PYX 2	50.06	1.69	1.68	0.57	18.71	0.33	13.96	12.56	0.07	0.01	99.64
PYX 3	53.39	0.76	1.96	0.94	16.57	0.27	24.87	1.76	0.01	0.01	100.53
PYX 4	51.69	0.86	0.90	0.46	24.94	0.39	18.58	2.39	n.d.	n.d.	100.21
PYX 5	55.43	0.45	1.67	0.73	11.96	0.18	29.17	1.32	0.01	0.01	100.94
PYX 6	51.73	0.93	1.26	0.78	20.88	0.37	19.21	4.54	0.02	n.d.	99.72
PYX 7	54.38	0.43	1.02	0.65	14.12	0.25	27.62	1.44	0.01	0.01	99.93
PYX 8	54.39	0.47	2.97	1.06	10.01	0.17	29.99	1.25	0.01	n.d.	100.32
PYX 9	55.32	0.39	1.12	0.60	13.47	0.21	27.97	1.42	n.d.	n.d.	100.50
PYX 10	50.30	1.11	1.52	0.83	19.34	0.36	16.23	9.31	0.08	n.d.	99.07
PYX 11	50.02	1.76	2.02	0.95	16.14	0.36	14.40	14.25	0.08	0.01	99.99
PYX 12	55.83	0.24	1.41	0.66	9.97	0.21	31.05	1.19	n.d.	n.d.	100.57
PYX 13	53.26	0.78	1.83	0.93	16.75	0.24	24.67	1.80	n.d.	0.01	100.28
PYX 14	54.99	0.39	1.37	0.67	12.13	0.17	28.80	1.33	0.01	n.d.	99.86
PYX 15	51.25	0.86	1.33	0.73	21.40	0.33	21.44	2.15	n.d.	n.d.	99.50
PYX 16	48.32	1.26	1.56	0.38	25.38	0.48	10.32	11.55	0.05	n.d.	99.30
PYX 17	53.12	0.68	2.89	1.03	12.59	0.20	27.48	1.41	n.d.	n.d.	99.40
PYX 18	48.24	1.02	1.13	0.29	24.21	0.45	10.07	13.06	0.05	n.d.	98.52
PYX 19	53.86	0.61	2.63	0.94	11.67	0.18	28.73	1.37	n.d.	n.d.	99.99
PYX 20	53.18	0.62	3.55	1.09	10.72	0.20	28.72	1.28	n.d.	0.02	99.38
PYX 21	51.63	0.80	1.79	1.00	18.84	0.32	22.58	2.00	n.d.	n.d.	98.97
PYX 22	53.32	0.67	3.23	1.09	11.77	0.19	28.32	1.30	n.d.	n.d.	99.89
PYX 23	49.84	1.46	1.67	0.50	19.03	0.33	13.18	13.35	0.08	n.d.	99.43
PYX 24	49.46	1.74	2.06	0.86	17.06	0.37	14.30	12.97	0.06	n.d.	98.87
PYX 25	52.35	0.67	2.33	0.96	14.10	0.20	26.66	1.59	0.02	n.d.	98.88
PYX 26	46.81	1.33	2.10	0.42	31.82	0.49	10.80	4.58	0.04	n.d.	98.37
PYX 27	47.23	0.89	1.18	0.31	31.85	0.58	8.78	7.43	0.01	0.01	98.27
PYX 28	52.54	0.63	3.71	1.08	10.43	0.22	29.03	1.22	0.02	0.00	98.88
PYX 29	53.39	0.59	2.76	0.96	12.40	0.19	27.94	1.53	0.01	n.d.	99.76
PYX 30	48.81	1.01	1.26	0.63	21.73	0.37	17.14	5.00	0.03	n.d.	95.98
PYX 31	53.62	0.59	2.93	0.97	11.22	0.20	28.73	1.36	n.d.	n.d.	99.62
PYX 32	54.97	0.30	1.28	0.64	10.97	0.20	30.22	1.20	0.02	n.d.	99.81
PYX 33	49.96	1.64	2.17	1.16	15.55	0.35	14.86	13.46	0.10	n.d.	99.26
PYX 34	49.70	1.66	1.94	0.77	16.78	0.34	14.41	13.72	0.09	0.02	99.43
PYX 35	49.22	1.53	1.77	0.42	17.43	0.29	11.43	17.08	0.06	0.01	99.24

n.d., not detected.

calculate the partition coefficient for a particular element for each individual pyroxene composition. In Equation 4 N_A is Avogadro's number, r_j (eightfold atomic radii of element j), and D_j is the partition coefficient for element j:

$$D_j = D_0 \cdot \exp\left\{\frac{-4\pi E N_A}{RT}\left[\frac{r_0}{2}(r_j - r_0)^2 + \frac{1}{3}(r_j - r_0)^3\right]\right\} \quad (4)$$

Using this method removes complications, such as imperfect matrix matching, etc., when using partition coefficients selected from the literature. Partition coefficients were then used to calculate the pyroxene equilibrium liquids. Pyroxene equilibrium liquids were initially calculated at 1350°C; this temperature was chosen as it was within the range of temperatures used by Sun and Liang (2013) for the experimentally calculated partition coefficients.

Plagioclase trace element partition coefficients were calculated after the method of Hui et al. (2011, and references therein) using Equation 5:

$$RT \ln D_i^{plag} = a_i X_{An} + b_i \quad (5)$$

D_i^{plag} is the calculated plagioclase partition coefficient for element "I", X_{An} is the anorthite content of the plagioclase, and a_i and b_i are fitting parameters (found by fitting Equation 5 to literature data that do not include any experiments using doped charges). The

Table 2. Plagioclase major and minor element compositions by electron probe micro analysis (wt% oxide).

	SiO_2	TiO_2	Al_2O_3	Cr_2O_3	FeO	MnO	MgO	CaO	Na_2O	K_2O	Total
Plag 1	46.29	0.06	34.90	n.d.	0.36	n.d.	0.18	17.73	1.39	0.11	101.01
Plag 2	45.75	0.03	35.03	0.01	0.31	0.03	0.19	17.85	1.31	0.10	100.60
Plag 3	46.31	0.06	34.53	n.d.	0.29	0.03	0.17	17.63	1.32	0.11	100.46
Plag 4	45.42	0.01	35.26	0.02	0.36	0.03	0.13	18.51	1.02	0.06	100.82
Plag 5	46.43	0.09	34.38	0.00	0.33	0.02	0.20	17.55	1.33	0.09	100.42
Plag 6	46.36	0.05	34.62	0.01	0.43	0.03	0.18	17.87	1.34	0.09	100.98
Plag 7	45.82	0.02	34.70	0.01	0.26	0.03	0.21	17.70	1.28	0.08	100.09
Plag 8	49.43	0.12	31.65	0.00	0.46	0.00	0.17	15.04	2.45	0.28	99.59
Plag 9	45.02	0.05	33.04	0.01	2.46	0.01	0.15	16.77	1.53	0.13	99.16
Plag 10	47.52	0.11	33.16	n.d.	0.37	0.01	0.21	16.28	1.91	0.17	99.73
Plag 11	47.51	0.08	33.36	0.03	0.39	n.d.	0.15	16.43	1.90	0.19	100.04
Plag 12	45.23	0.06	35.22	0.04	0.33	0.03	0.19	17.69	1.34	0.09	100.22
Plag 13	44.48	0.07	35.59	0.02	0.32	n.d.	0.21	17.96	1.19	0.08	99.92
Plag 14	46.63	0.10	33.97	0.00	0.55	0.02	0.16	16.85	1.67	0.15	100.12
Plag 15	45.29	0.04	35.09	n.d.	0.32	0.01	0.16	18.06	1.12	0.08	100.17
Plag 16	45.40	0.03	34.91	0.02	0.43	0.02	0.15	18.03	1.18	0.11	100.26
Plag 17	46.49	0.06	34.31	n.d.	0.51	n.d.	0.16	17.47	1.39	0.12	100.52
Plag 18	46.02	0.04	34.78	0.03	0.29	n.d.	0.25	17.66	1.37	0.10	100.54
Plag 19	46.91	0.10	33.89	0.00	0.49	0.01	0.20	16.75	1.79	0.16	100.31
Plag 20	46.70	0.13	34.22	0.03	0.39	0.01	0.19	16.85	1.72	0.15	100.39
Plag 21	46.14	0.06	34.55	0.02	0.53	n.d.	0.17	17.28	1.57	0.14	100.46
Plag 22	45.17	0.05	35.83	n.d.	0.26	n.d.	0.22	17.99	1.22	0.08	100.85
Plag 23	45.93	0.07	34.57	n.d.	0.43	0.02	0.17	17.01	1.66	0.17	100.02
Plag 24	46.83	0.10	33.58	n.d.	0.51	n.d.	0.18	16.27	2.03	0.18	99.68
Plag 25	48.79	0.03	32.21	n.d.	1.11	0.01	0.08	15.54	1.82	0.72	100.31
Plag 26	46.46	0.08	34.47	n.d.	0.40	0.02	0.14	17.17	1.63	0.16	100.54
Plag 27	46.07	0.05	35.26	0.01	0.60	n.d.	0.14	17.73	1.29	0.12	101.26
Plag 28	46.86	0.08	34.29	n.d.	0.55	0.04	0.13	17.20	1.62	0.18	100.95
Plag 29	49.06	0.14	32.43	0.02	0.64	0.02	0.16	15.54	2.30	0.30	100.62
Plag 30	46.18	0.07	34.51	0.01	0.41	0.01	0.16	17.23	1.57	0.13	100.29
Plag 31	46.87	0.06	34.28	n.d.	0.34	n.d.	0.20	17.28	1.62	0.16	100.81
Plag 32	45.53	0.07	33.10	n.d.	0.30	0.01	0.19	16.94	1.57	0.13	97.83
Plag 33	44.83	0.07	35.11	n.d.	0.36	n.d.	0.16	17.90	1.30	0.10	99.83
Plag 34	45.78	0.07	34.68	0.03	0.44	0.02	0.16	17.35	1.56	0.13	100.22
Plag 36	45.38	0.04	34.94	n.d.	0.41	0.02	0.16	17.97	1.24	0.09	100.25
Plag 37	47.89	0.09	33.17	n.d.	0.50	0.02	0.19	16.10	2.10	0.19	100.27
Plag 38	45.19	0.05	35.31	n.d.	0.23	n.d.	0.22	17.79	1.30	0.10	100.18
Plag 39	45.25	0.04	35.31	0.02	0.38	0.01	0.20	17.83	1.26	0.11	100.43
Plag 40	45.72	0.05	35.09	0.01	0.28	n.d.	0.21	17.72	1.38	0.09	100.54
Plag 41	45.40	0.06	34.97	0.03	0.32	nd	0.16	17.79	1.34	0.10	100.18
Plag 42	43.95	0.07	36.12	0.00	0.34	n.d.	0.16	18.84	0.89	0.05	100.42
Plag 43	44.12	0.05	36.03	n.d.	0.24	0.01	0.16	18.52	0.95	0.07	100.14
Plag 44	46.82	0.05	34.05	n.d.	0.40	0.02	0.22	17.09	1.75	0.13	100.54
Plag 45	46.66	0.10	34.17	n.d.	0.44	0.04	0.22	16.99	1.60	0.13	100.34
Plag 46	46.18	0.03	34.48	0.01	0.26	0.03	0.23	17.63	1.40	0.11	100.37
Plag 47	46.95	0.13	33.97	0.02	0.38	0.01	0.20	16.90	1.64	0.14	100.34
Plag 48	46.24	0.05	34.55	0.01	0.48	n.d.	0.14	17.27	1.59	0.15	100.47
Plag 49	45.10	0.07	35.51	n.d.	0.30	0.01	0.13	18.16	1.14	0.07	100.50
Plag 50	45.63	0.10	35.10	0.01	0.40	0.01	0.19	17.61	1.42	0.10	100.57
Plag 51	45.33	0.10	35.24	n.d.	0.30	n.d.	0.20	17.87	1.25	0.07	100.37

n.d., not detected.

dependence of D_i^{plag} on anorthite content of plagioclase has been previously demonstrated (e.g., Blundy and Wood 1991; Bindeman et al. 1998; Bédard 2006; Tepley et al. 2010). Partition coefficients are then calculated on the basis of composition, using the An content as measured by EPMA.

Equation 6 was used to calculate Opx and plagioclase equilibrium liquids using the D values derived using the methods described above.

$$\frac{C_c^i}{D_c^i} = C_0^i \quad (6)$$

Where C_c^i is the concentration of element "I" in a crystal in ppm, D_c^i is the partition coefficient, and C_0^i is the concentration of element "I" in the liquid from which the crystal formed.

Cooling rates were approximated using plagioclase, following the methods of Grove and Walker (1977). The minor axes of the best-fit ellipses (calculated during crystal size distribution construction) were used for the width of plagioclase, and represent a minimum estimate of cooling rate.

RESULTS

Major element compositions of the Opx crystals form a coherent trend evolving from enstatite to pigeonite and become more Fe-rich, but the trend becomes more scattered with increasing Ca close to the rims (Table 1, Fig. 2). Laser ablation analyses of the large pyroxene crystals are focused on enstatite areas (Fig. 2) as they were the only sites large enough to allow quantitative analyses by LA-ICP-MS. Plagioclase major element compositions can be found in Table 2.

The Opx REE profiles are depleted in the light (L) REE (Fig. 3, Table 3). The Opx equilibrium liquids (Table 4, corresponding partition coefficients can be found in Table 5) calculated at 1350 °C display relatively flat REE profiles (Fig. 3), whereas the 15434,181 WR profile (in red) displays the slightly negative slope from the LREE to heavy (H)REE typical of KREEP basalts (e.g., Shih 1977). The LREE values for Opx equilibrium liquids and the WR are similar, slopes of the LREE being subparallel between the Opx equilibrium liquids and the WR. However, this is not the case for the HREE. Overall, Opx equilibrium liquids are enriched in HREE relative to the WR and the profiles are relatively flat (Fig. 3).

Opx equilibrium liquid abundances for Zr and Hf show that the Zr/Hf ratios of the liquids (average of 42.5) are similar to 15434,181 WR (41.0—Simon et al. 1988), bulk Moon (44.8—e.g., Taylor 1982), and chondritic values (37.9—Anders and Grevesse 1989). The results indicate that ilmenite was not crystallizing with or prior to Opx, as Hf and Zr would only fractionate if significant ilmenite was extracted (e.g., McKay et al. 1986; Neal 2001).

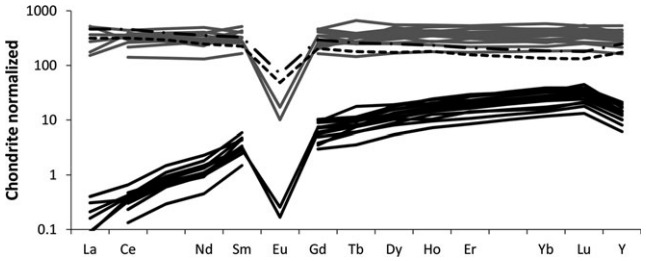

Fig. 3. Chondrite-normalized REE plots. Pyroxene mineral REE + Y data in black. The black-dashed line is the 15434,181 whole rock (WR) composition from Simon et al. (1988). The black-doted/dashed line is the Opx-subtracted WR composition calculated by subtracting the weighted average trace element content of the measured Opx crystals coupled with the Opx modal abundance (as observed in the thin section 181) from the WR composition reported by Simon et al. (1988). Pyroxene REE + Y equilibrium liquids in gray (as calculated at 1350 °C). Chondrite REE data from Anders and Grevesse (1989).

Plagioclase trace element data (Fig. 4, Table 3) were used to calculate equilibrium liquid REE compositions (Table 4) using partition coefficients derived using the method described by Hui et al. (2011). Plagioclase equilibrium liquids encompass and are subparallel to the WR composition of 15434,181 (Fig. 4, Table 4).

DISCUSSION

The WR composition of 15434 is a product of all processes affecting the sample. Therefore, if a mineral (such as Opx or plagioclase) crystallizes (via fractional crystallization) early from a magma, it should have a REE liquid composition generally lower than, and subparallel to, that of the WR. Late-forming phases will crystallize from liquids with higher equilibrium liquid REE concentrations than the average represented by the WR, with the REE profile again being subparallel to that of the WR. Phenocrysts would form early (as they would have room to grow) and Opx is typically an early crystallizing phase in magmas with relatively high silica activity. It follows that the Opx equilibrium liquids should plot below the WR REE profile. This is not the case as the LREE abundances are similar, and the profiles are subparallel to those of the WR, and are enriched in the middle and heavy REEs (Fig. 3).

The cores of the large Opx crystals remain somewhat of a mystery, as they do not appear to have a direct relationship with the WR REE composition of 15434 (Fig. 3). This would make them "tramp" crystals of some sort (antecrysts if they are distantly related to the WR, or xenocrysts if they are unrelated; see Wright and Fiske 1971; and Marsh [2013]; for definition of "tramp" crystal). If correct, then the WR composition (Simon et al. 1988) does not represent a true magmatic

Table 3. Pyroxene and plagioclase trace element data (ppm).

	Ti	Co	Y	Zr	La	Ce	Pr	Nd	Sm	Eu	Gd	Tb	Dy	Ho	Er	Yb	Lu	Hf
PYX 1	8978.78	34.35	33.10	27.14	0.09	0.40	0.08	1.04	0.64	n.d.	1.82	0.64	4.62	1.18	4.29	6.28	0.94	1.38
PYX 7	4025.49	32.38	15.52	8.49	n.d.	0.14	<0.037	0.44	0.36	n.d.	0.69	0.27	2.48	0.52	2.25	2.56	0.52	0.36
PYX 8	5655.53	36.08	22.78	24.58	n.d.	0.22	<0.046	0.42	0.67	n.d.	1.09	0.28	3.05	0.86	2.89	4.16	0.83	0.88
PYX 9	4250.63	38.09	15.90	9.22	n.d.	0.18	<0.045	0.45	<0.23	n.d.	0.75	0.22	2.14	0.64	2.18	2.80	0.50	0.43
PYX 12	2237.55	28.67	9.51	6.69	n.d.	0.08	0.04	0.21	0.22	n.d.	0.59	0.13	1.31	0.36	1.34	1.90	0.32	0.32
PYX 14	4401.87	29.99	20.14	20.49	0.02	0.23	0.07	0.64	0.42	n.d.	1.39	0.30	2.70	0.75	2.68	3.86	0.66	0.93
PYX 19	4629.44	30.74	22.94	25.71	0.04	0.24	0.07	0.67	0.44	n.d.	1.46	0.28	3.26	0.87	3.17	4.53	0.73	1.30
PYX 20	5146.49	30.30	27.65	32.21	0.07	0.21	0.07	0.50	0.42	n.d.	1.96	0.40	3.76	0.97	3.50	5.19	0.79	1.68
PYX 22	3688.71	28.30	18.75	20.97	0.02	0.20	0.06	0.60	0.48	0.01	1.18	0.29	2.58	0.72	2.59	3.66	0.58	0.98
PYX 25	5895.95	36.21	30.69	28.74	n.d.	0.25	0.07	0.82	0.86	n.d.	2.01	0.41	4.29	1.22	4.67	5.38	0.85	1.27
PYX 28	3850.78	30.24	22.00	23.90	0.05	0.26	0.08	0.65	0.43	0.01	1.43	0.34	3.19	0.80	2.87	4.13	0.68	1.06
PYX 29	5684.53	36.27	30.24	30.21	n.d.	0.26	0.06	0.62	0.70	n.d.	1.99	0.33	4.63	1.01	4.24	5.72	0.93	1.48
PYX 31	4946.92	32.59	26.16	27.72	n.d.	0.28	0.13	0.48	0.50	n.d.	1.75	0.36	3.79	1.03	3.63	5.25	1.08	1.29
PYX 32	3004.20	31.22	12.51	7.31	0.10	n.d.	0.05	n.d.	0.24	n.d.	0.97	0.22	1.95	0.48	1.69	2.31	0.43	0.47
Plag 2	467.87	1.82	0.43	2.91	5.87	0.72	2.94	0.61	3.09	0.52	0.08	0.28	0.06	0.11	0.04	0.15	n.d.	n.d.
Plag 6	408.00	1.96	2.42	3.52	6.94	0.90	3.34	0.52	3.48	0.39	0.11	0.49	0.08	0.21	0.02	0.40	n.d.	0.10
Plag 7	367.47	1.86	0.73	3.25	6.93	0.78	3.50	0.63	3.16	0.64	0.05	0.45	0.04	0.15	0.02	0.20	n.d.	n.d.
Plag 18	392.61	2.25	0.52	3.50	6.70	0.75	3.69	0.50	3.25	0.68	0.06	0.44	0.07	0.12	0.03	n.d.	n.d.	n.d.
Plag 24	809.24	2.13	0.78	3.62	7.74	0.88	3.69	0.57	3.77	0.51	0.09	0.48	0.11	0.16	0.04	0.17	n.d.	n.d.
Plag 28	453.26	2.03	0.14	3.43	7.16	0.83	4.43	0.84	2.98	0.63	0.07	0.35	0.04	0.19	n.d.	0.15	n.d.	n.d.
Plag 32	452.27	2.04	0.44	3.89	7.70	1.00	3.89	0.89	3.82	0.70	0.05	0.45	0.08	0.18	n.d.	n.d.	n.d.	0.02
Plag 46	636.64	2.35	0.73	3.43	6.97	0.86	3.09	0.53	3.11	0.77	0.07	0.50	0.08	0.23	0.03	0.32	n.d.	0.05

n.d., not detected.

Table 4. Calculated equilibrium liquids (ppm).

	Ti	Y	Zr	La	Ce	Pr	Nd	Sm	Eu	Gd	Tb	Dy	Ho	Er	Yb	Lu	Hf
PYX 1	172909	833.8	4779	119.73	265.48	28.28	224.51	59.05	–	89.76	24.06	134.34	27.78	84.54	94.66	12.82	126.1
PYX 7	84630	436.1	1381	–	129.93	–	120.69	39.85	–	39.30	11.58	80.98	13.68	48.97	42.28	7.75	31.2
PYX 8	85528	521.7	2770	–	198.03	–	103.02	63.33	–	51.57	9.77	81.40	18.32	51.13	55.92	10.15	52.5
PYX 9	91482	470.7	1544	–	180.11	–	131.06	–	–	45.11	9.70	73.65	17.61	49.94	48.62	7.82	38.0
PYX 12	42227	253.3	848	–	85.23	19.27	59.28	24.25	–	32.35	5.27	40.68	9.01	27.50	29.63	4.54	21.5
PYX 14	88007	567.0	3058	41.22	228.12	37.18	183.99	48.14	–	80.35	12.66	88.50	19.56	58.29	63.61	9.88	73.5
PYX 19	61384	516.0	2946	85.58	217.66	36.66	157.26	40.87	0.96	68.84	12.18	87.08	17.51	52.07	56.92	8.45	68.6
PYX 20	73099	611.0	3657	122.79	176.51	28.14	115.97	37.95	–	89.19	13.56	96.79	19.90	59.74	67.21	9.26	100.2
PYX 22	69335	524.7	3479	63.82	197.65	28.74	158.97	40.88	–	68.61	9.74	86.85	18.43	55.99	60.63	8.86	85.2
PYX 25	96794	695.5	3861	–	181.09	26.99	177.23	75.62	–	91.54	14.07	112.74	25.81	82.26	72.22	10.28	89.5
PYX 28	49607	390.1	2205	35.60	158.60	23.51	133.54	40.93	0.56	50.64	9.16	62.56	13.99	41.61	44.64	6.45	54.0
PYX 29	88330	679.5	3710	–	198.07	24.55	138.06	62.26	–	90.64	11.26	120.82	21.10	73.94	76.00	11.19	95.6
PYX 31	75796	600.3	3300	–	238.29	54.23	113.79	46.49	–	82.32	12.55	101.22	22.04	64.43	70.80	13.21	80.9
PYX 32	57718	333.9	966	207.23	–	27.57	–	26.17	–	53.59	8.99	60.68	11.96	34.80	36.07	6.12	33.0
Plag 2	–	–	–	88.01	198.16	26.77	122.04	38.38	4.43	40.12	7.98	34.43	10.58	28.95	106.07	–	–
Plag 6	–	–	–	104.86	231.35	33.13	136.60	32.15	4.99	29.52	10.83	57.80	13.11	54.28	264.72	–	–
Plag 7	–	–	–	99.87	237.06	29.50	147.58	40.37	4.53	50.67	5.64	56.02	6.89	40.90	149.47	–	–
Plag 18	–	–	–	101.61	218.61	26.77	147.15	30.01	4.66	50.41	6.20	50.37	10.85	29.90	n.d.	–	–
Plag 24	–	–	–	69.28	178.69	21.77	97.81	21.21	5.40	22.77	4.75	29.89	8.89	17.10	17.18	–	–
Plag 28	–	–	–	83.97	202.80	25.53	149.48	41.46	4.27	37.64	5.18	31.48	4.90	33.91	42.02	–	–
Plag 32	–	–	–	97.97	223.28	31.46	134.96	45.38	5.47	43.65	3.77	42.15	9.88	34.42	n.d.	–	–
Plag 46	–	–	–	97.31	223.12	30.34	120.47	30.98	4.46	55.51	6.30	55.75	11.37	55.37	174.99	–	–

–, abundance not calculated due to either lack of abundance data and/or lack of partition coefficient.
n.d., not detected.

signature, so the Opx-subtracted WR REE profile is also presented in Figs. 3, 4, and 5. We also note that the model used to produce the pyroxene D values is highly sensitive to temperature (Yao et al. 2012; Sun and Liang 2013). By lowering the temperature used to calculate the partition coefficients, the slope of the REE

Table 5. Opx partition coefficients.

	Ti	Y	Zr	La	Ce	Pr	Nd	Sm	Eu	Gd	Tb	Dy	Ho	Er	Yb	Lu	Hf
PYX 1	0.0519	0.0397	0.0057	0.0008	0.0015	0.0027	0.0046	0.0108	0.0150	0.0203	0.0267	0.0344	0.0425	0.0507	0.0663	0.0732	0.0109
PYX 7	0.0476	0.0356	0.0061	0.0005	0.0011	0.0020	0.0036	0.0090	0.0128	0.0176	0.0235	0.0306	0.0382	0.0459	0.0606	0.0670	0.0117
PYX 8	0.0661	0.0437	0.0089	0.0005	0.0011	0.0022	0.0041	0.0106	0.0152	0.0211	0.0286	0.0375	0.0469	0.0565	0.0744	0.0821	0.0168
PYX 9	0.0465	0.0338	0.0060	0.0005	0.0010	0.0019	0.0034	0.0085	0.0121	0.0166	0.0223	0.0291	0.0363	0.0437	0.0576	0.0637	0.0113
PYX 12	0.0530	0.0375	0.0079	0.0005	0.0009	0.0019	0.0035	0.0090	0.0130	0.0181	0.0245	0.0322	0.0404	0.0486	0.0641	0.0707	0.0148
PYX 14	0.0500	0.0355	0.0067	0.0005	0.0010	0.0019	0.0035	0.0088	0.0125	0.0173	0.0233	0.0305	0.0382	0.0460	0.0607	0.0671	0.0127
PYX 19	0.0627	0.0426	0.0081	0.0006	0.0012	0.0023	0.0041	0.0105	0.0150	0.0208	0.0280	0.0366	0.0458	0.0551	0.0726	0.0801	0.0154
PYX 20	0.0704	0.0453	0.0088	0.0006	0.0012	0.0023	0.0043	0.0111	0.0158	0.0220	0.0296	0.0388	0.0487	0.0586	0.0772	0.0853	0.0168
PYX 22	0.0668	0.0437	0.0082	0.0006	0.0012	0.0023	0.0042	0.0108	0.0154	0.0213	0.0287	0.0375	0.0470	0.0566	0.0747	0.0826	0.0156
PYX 25	0.0609	0.0441	0.0074	0.0007	0.0014	0.0026	0.0046	0.0114	0.0160	0.0220	0.0293	0.0381	0.0473	0.0568	0.0745	0.0822	0.0142
PYX 28	0.0744	0.0481	0.0095	0.0006	0.0012	0.0024	0.0045	0.0117	0.0167	0.0233	0.0314	0.0412	0.0517	0.0622	0.0820	0.0905	0.0181
PYX 29	0.0644	0.0445	0.0081	0.0006	0.0013	0.0025	0.0045	0.0112	0.0159	0.0220	0.0294	0.0383	0.0478	0.0573	0.0753	0.0831	0.0155
PYX 31	0.0653	0.0436	0.0084	0.0006	0.0012	0.0023	0.0042	0.0108	0.0153	0.0213	0.0286	0.0374	0.0468	0.0563	0.0742	0.0819	0.0159
PYX 32	0.0520	0.0375	0.0076	0.0005	0.0010	0.0019	0.0035	0.0091	0.0130	0.0181	0.0245	0.0321	0.0403	0.0486	0.0640	0.0707	0.0142

Calculated at 1350 °C.

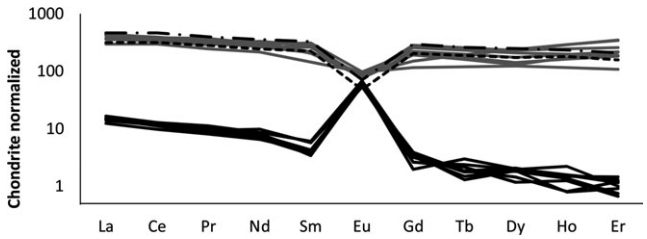

Fig. 4. Plagioclase chondrite-normalized REE data. Plagioclase mineral REE data normalized to chondrite in black. As in Fig. 3, the black-dashed line is 15434,181 whole rock (WR) from Simon et al. (1988) and the black-dotted/dashed line is the Opx-subtracted WR composition. Plagioclase equilibrium liquid REE data normalized to chondrite in gray. Chondrite REE data from Anders and Grevesse (1989).

profile can be changed. Changing the temperature from 1350 °C to 1250 °C produces equilibrium liquid REE profiles that are more "KREEP-like" (compare Fig. 3 with Fig. 5a), but higher relative to the WR and Opx-subtracted WR values. If the temperature is progressively lowered to 1050 °C, the Opx equilibrium liquids are no longer distinct from the Opx-subtracted WR composition, and would likely represent an accumulation of phenocrysts (Fig. 5a–e). If this is the case, then the Opx-subtracted WR composition would represent the true liquid composition (Figs. 3 and 5a, 5f). Therefore, the temperature at which the Opx formed is key to determining whether the Opx are phenocrysts or xenocrysts/antecrysts. Apollo 15 KREEP basalt 15386 reached its liquidus at 1200 °C to 1180 °C, and at 1172 °C began to crystallize low-Ca Pyroxene, high-An plagioclase, and olivine (Rutherford et al. 1996). Furthermore, temperatures calculated for Opx, using major element compositions from the reported WR composition and the high-K KREEP composition of Warren (1989) as an approximation for the Opx-subtracted WR (high-K KREEP and the Opx-subtracted WR are very similar in REE, Y, Ti, Zr, and Hf abundances; e.g., Fig. 5f) using the methods of Putirka (2008) (iteratively solving equations 28a and 29c).

We constructed a series of figures plotting $[Ce/Sm]_N$ versus $[Gd/Yb]_N$ ratios (Fig. 5b–e) to compare each of the Opx equilibrium liquids to the Opx-subtracted WR in 100 °C increments starting at 1350 °C and decreasing to 1050 °C. Crystallization temperatures varied from 1167 °C to 1274 °C (average 1230 °C) using 15434,181 WR, and from 1145 °C to 1243 °C (average 1206 °C) using Warren (1989) high-K KREEP as the parental magma when calculated using the methods of Putirka (2008). If the Opx crystals are phenocrysts, then the calculated temperature for Opx saturation should be approximately 1050 °C (Fig. 5a and e); the temperature calculations and experimental work using 15386 (Rutherford et al. 1996), however, range in temperature from 1274 °C to 1145 °C, and thus remain distinct from the Opx-subtracted WR (Fig. 5c and 5d). This result is inconsistent with Opx being a true phenocryst phase in 15434,181.

Unlike the pyroxenes, the plagioclase equilibrium liquid REE profiles are subparallel to that of the WR and the Opx-subtracted WR, but plot equal to or below it (Fig. 4). This observation is consistent with plagioclase being a relatively early crystallizing phase. With the equilibrium liquids of the Opx crystals suggesting it is a relatively late-stage phase (i.e., they plot at or above the Opx-subtracted WR values—Fig. 3), the large Opx crystals are then "tramp" crystals and thus the liquid the plagioclase formed from would be the Opx-subtracted WR, similar to high-K KREEP (Warren 1989; Fig. 5f).

The compositional variation seen in constituent phases is particularly important when considering the petrogenesis of 15434,181. The large Mg-rich, Ca-poor pyroxenes contain increasing Fe and Ca found toward the rims to form Fe-pigeonite-to-augite overgrowths (Figs. 1c and 2). This variation could be due to limited fractional crystallization in a magma chamber (Taylor et al. 2012). The magma chamber is possibly formed as a lopolith or laccolith in the crust of the Moon at a point of neutral buoyancy (cf. Wieczorek et al. 2001). However, the original two-stage cooling history invoked for 15434,181 (Ryder 1987) is not required if the large Opx crystals are tramp crystals. The data presented here are consistent with the Opx crystals being a product of an earlier and unrelated magma experiencing relatively slow cooling. These Opx were then incorporated into the 15434,181 parent magma. If pigeonite–augite overgrowths and plagioclase cocrystallized, this could explain the observations of plagioclase laths penetrating the outer portions (Fig. 1b, 1c) of the large pyroxene crystals. Relatively rapid cooling produced the plagioclase laths, with average rates of approximately 4.3 °C h^{-1}, calculated following the Grove and Walker (1977) method (Fig. 6). This suggests two things (1) the majority of plagioclase crystals began crystallizing on the lunar surface and (2) the rate of cooling for the plagioclase is not consistent with the plagioclase-pyroxene intergrowths, unless the pigeonite–augite overgrowths are also formed on the lunar surface during lava flow crystallization.

In addition to plagioclase being intergrown with pigeonite–augite, in some instances, it is also intergrown with Opx. Notably, the plagioclase data form two distinct compositional groups (Fig. 7). The analyzed plagioclase found as intergrowths in the Opx are all

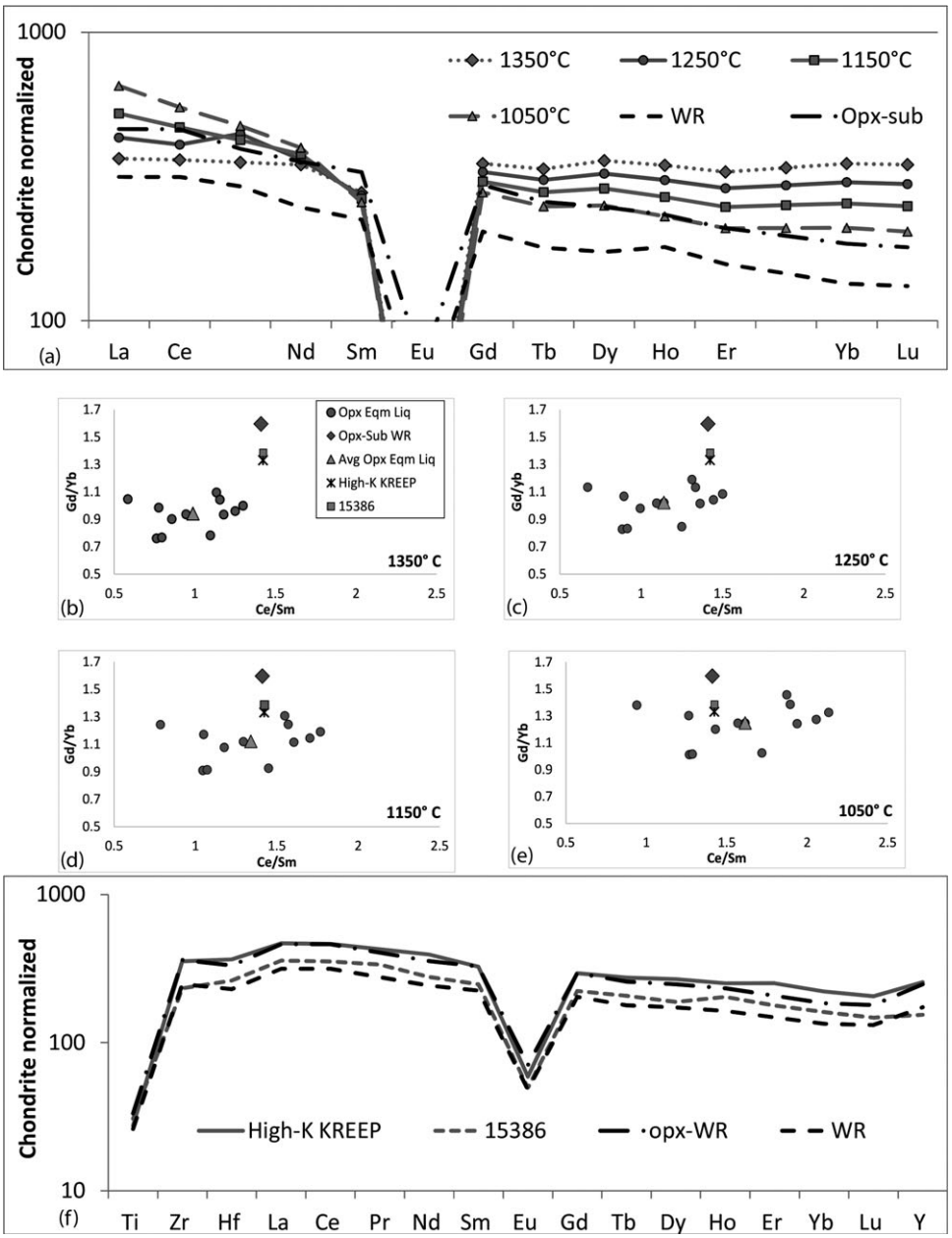

Fig. 5. a) Pyroxene REE equilibrium liquid of PX19 normalized to chondrite and calculated in 100 °C increments starting at 1050 °C and going to 1350 °C. Liquids calculated at 1250 °C are more KREEP-like than 1350 °C but enriched above and subparallel to the whole rock (WR) and Opx-subtracted WR. Liquids calculated at 1050 °C are KREEP-like and parallel to and consistent with the OPX-subtracted WR. Chondrite REE data from Anders and Grevesse (1989). (b, c, d, and e): $[Ce/Sm]_N$ versus $[Gd/Yb]_N$ plots of the Opx equilibrium liquids in 100 °C intervals: Opx-subtracted WR—diamond; average Opx equilibrium liquid—triangle; KREEP basalt 15386 included for comparison as it is the best known pristine/endogenous KREEP basalt (composition from Neal and Kramer 2003, 2006)—square; high-K KREEP from Warren (1989)—X symbol. Opx equilibrium liquids from 1350 °C to 1150 °C (b, c, and d) are distinct from the Opx-subtracted WR. At 1050 °C (e), the Opx equilibrium liquids are consistent from the Opx-subtracted WR. f) Chondrite-normalized REE plot showing the 15434,181 WR composition (Simon et al. 1988; black-dashed line), the Opx-subtracted WR composition (black-dotted/dashed line), high-K KREEP (Warren 1989; gray line), and KREEP basalt 15386 (Neal and Kramer 2003, 2006; Ti abundance from Vaniman and Papike [1980] gray dashed line). This diagram demonstrates the similarity between the Opx-subtracted WR and the high-K KREEP composition of Warren (1989). Chondrite REE data from Anders and Grevesse (1989).

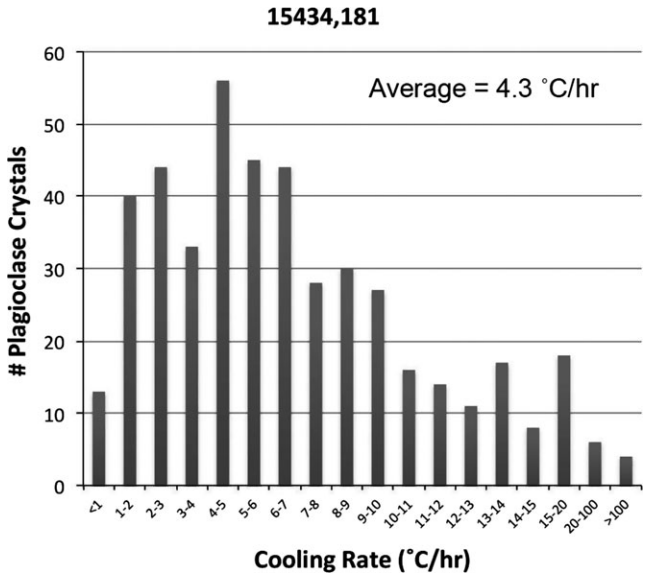

Fig. 6. Plagioclase cooling rate was calculated following Grove and Walker (1977) using the minor axis of plagioclase as measured by ImageJ (Schneider et al. 2012) during crystal size distribution analysis (Cronberger and Neal 2013). The average cooling rate is 4.3 °C h^{-1}.

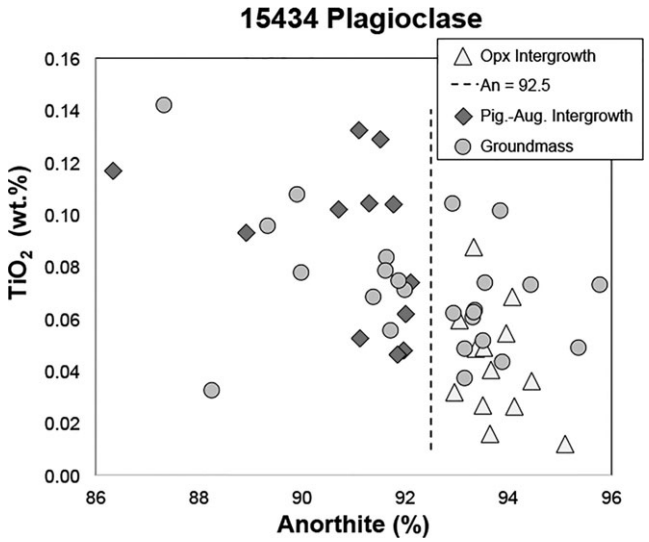

Fig. 7. TiO_2 (wt%) versus An plot for plagioclase in 15434,181: Note the gap at An 92.5 defined by the dashed line. Compositions of penetrative plagioclase intergrowths with Opx shown as triangles, plagioclase intergrown with pigeonite–augite are shown as diamonds, and groundmass plagioclase as circles.

found within the higher An grouping (>$An_{92.5}$ highlighted in Fig. 7). This relationship indicates that either initially the 15434 parent magma crystallized Opx (as an overgrowth on the large crystals) and high-An plagioclase (along with high-An plagioclase in the groundmass; Fig. 7), or the intergrown plagioclase crystals were formed with the Opx crystals from an unrelated magma (see below). The remaining lower An plagioclases are formed subsequently within the groundmass and pigeonite–augite overgrowths, probably on the lunar surface post eruption.

In order to compare the 15434 equilibrium liquid data with KREEP basalts, we compiled a list of all KREEP basalt analyses from the literature for Ce (representative of the LREE), Zr, and Hf. This compilation omitted data were analyzed by instrumental neutron activation (INA). Due to the poor sensitivity, accuracy, and precision of INA in quantifying Zr, especially in the 1970–2000 time frame when most of the analyses were undertaken, defining precise Zr/Hf ratios using these data is not possible. For example, Salpas et al. (1987) reported INA analyses of KREEP basalt clasts in Apollo 17 breccia 72275 and concluded they came from a unique source. The Zr/Hf ratio should exhibit relative uniformity but instead yields a chondritic average of 37.7, but with an error of ±9 (2-sigma). In Figs. 8a–c, the 15434 Opx equilibrium liquids are compared with high-K KREEP, the WR composition of 15434,181, and KREEP basalts (see figure caption for samples and data references). Equilibrium liquid Zr/Hf ratios (30.5–55.0, average of 42.5) overlap the WR and bulk Moon values (41.0 and ≈44.8, respectively; e.g., Taylor 1982). Increasing the Zr/Hf ratio of a magma to suprachondritic levels can be achieved by crystal fractionation of ilmenite (e.g., McKay et al. 1986; Nakamura et al. 1986), where Hf is slightly less incompatible in ilmenite than Zr. These ratios suggest that the equilibrium liquids either experienced ilmenite removal during Opx crystallization or they incorporated a component that had already experienced ilmenite fractionation. The WR Zr/Hf ratio is similar to the bulk Moon value and chondritic meteorites (e.g., Anders and Grevesse 1989) (Fig. 8a), suggesting that the 15434 parent magma did not crystallize ilmenite and that the Opx crystals are unrelated to the parent magma composition. As KREEP is formed after the removal of ilmenite from the LMO (e.g., Snyder et al. 1992; Elkins-Tanton et al. 2002, 2011), incorporation of a KREEP component during early Opx crystallization is a plausible explanation for the equilibrium liquid compositions. The Opx equilibrium liquids have approximately chondritic (37.9) Zr/Hf ratios (38.1–39.6) extending to suprachondritic values of 40.5–55.1. However, the WR Zr and Hf abundances are generally well below those of the equilibrium liquids (Fig. 8a). This discrepancy could be explained by late-stage crystallization of zircon. Dickinson and Hess (1982) concluded that

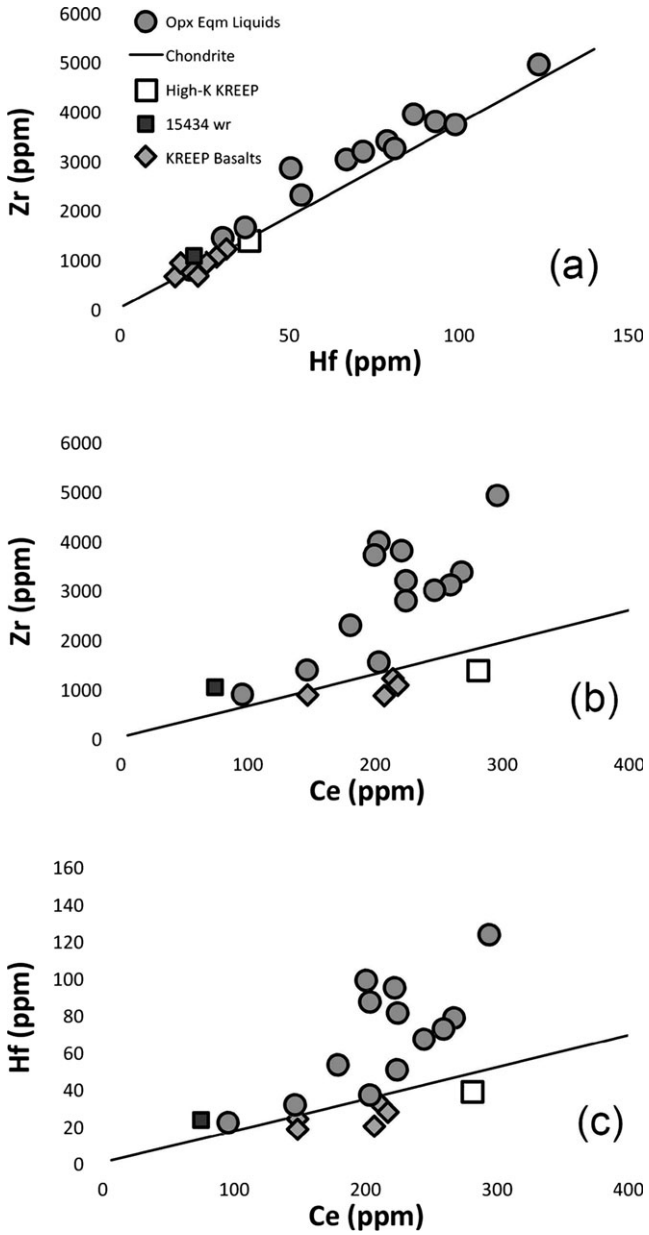

Fig. 8. Incompatible element relationships between the Opx equilibrium liquids (this study) compared to the chondritic ratio (Anders and Grevesse 1989), high-K KREEP (Warren 1989), the 15434 whole rock (WR) composition (Simon et al. 1988) and various KREEP basalts (Church et al. 1972; Vaniman and Papike 1980; Warren et al. 1983; Neal and Kramer 2006). Note that the majority of the Opx equilibrium liquids have suprachondritic Zr/Hf, Zr/Ce, and Hf/Ce ratios, as does the 15434 WR compositions. The KREEP basalts and high-K KREEP are at or below the chondritic ratio.

approximately 9000 ppm Zr was required to stabilize zircon in lunar basaltic magmas. Equilibrium liquid values for the early crystallizing Opx reach to over 5000 ppm (Fig. 8b), so having zircon crystallizing later in the sequence is feasible, which would move the WR Zr/Hf, Zr/Ce, and Hf/Ce back toward chondritic values (Fig. 8c). Clearly, the large Opx crystals in 15434,181 crystallized from a magma that was, for the most part, distinct from the compositions of known KREEP basalts.

Antecryst or xenocryst origin for Opx?

Opx equilibrium liquids and the Opx-subtracted WR could be distantly related. Opx equilibrium liquids (enriched over and subparallel to the Opx-subtracted WR; Fig. 3) could form the parental liquid of the Opx-subtracted WR, if the generally incompatible trace elements (REEs, Zr, Hf) were lowered by removal of minor phases (e.g., phosphates, zircon, etc.), to levels represented by the KREEP basalts (Fig. 8). Alternatively, the Opx formed were from an unrelated KREEP-rich liquid. In an attempt to distinguish between a xenocryst or antecryst origin for the large Opx crystals, a model was constructed to generate the Opx-subtracted WR from the most primitive Opx equilibrium liquid. If mineral phases that incorporate REEs such as phosphates, (particularly whitlockite, a common accessory mineral in KREEP basalts; e.g., Taylor et al. 2012) and zircon (as Zr is enriched within the equilibrium liquids and associated with KREEP basalts; e.g., Nemchin et al. 2008) were to crystallize, the resulting magma could have a REE profile similar to that of the WR. Using the equilibrium liquid calculated from pyroxene PX12 (which has the highest Mg#, and was likely the earliest of the measured Opx crystals to form) as the initial liquid, fractional crystallization modeling was conducted that removed varying abundances of pyroxene, plagioclase, whitlockite (*D* values from Jolliff et al. 1993), and zircon (*D* values from Irving and Frey 1984). However, this approach could not reproduce the Opx-subtracted WR. We therefore conclude that the large pyroxene crystals should be classified as xenocrysts because they are wholly unrelated to the WR. This conclusion has implications for the plagioclase crystals seen protruding into the Opx cores of these large crystals that fall within the high-An grouping (Fig. 7). As noted above, it is feasible that incorporation of the large Opx crystals into the 15434 parent magma resulted in an Opx overgrowth that graded into pigeonite and augite that cocrystallized with plagioclase. The caveat would be that as crystallization proceeded, the An content of the plagioclase decreased. Alternatively, these Opx-plagioclase intergrowths formed with the Opx crystals in a magma were unrelated to 15434, but had the same composition at the high-An groundmass plagioclase in 15434. Incorporation into the 15434 parent magma

resulted in pigeonite-to-augite overgrowths and cocrystallization of plagioclase of the low-An grouping. Initial crystallization of this latter scenario started with the high-An groundmass plagioclase followed by the pigeonite-to-augite overgrowths that cocrystallized with low-An plagioclase. On the basis of the data presented here, it is difficult to distinguish between these two crystallization environments.

CONCLUSIONS

Contrary to previous work on 15434,181 (and 188), the data reported here indicate that the large Opx crystals in KREEP basalt sample 15434, thin section 181, are not phenocrysts but xenocrysts. Therefore, the true WR composition should be that reported by Simon et al. (1988) with the contribution from the Opx xenocrysts removed. These Opx xenocrysts are likely to have formed at depth in their KREEPy parental liquid that was richer in incompatible trace elements relative to high-K KREEP, the 15434,181 WR composition, the Opx-subtracted WR composition, and what is typical of KREEP basalts. The Opx xenocrysts were then incorporated into the 15434,181 high-K KREEP-like parental magma. Petrographic and compositional relationships indicate plagioclase (with $An_{>92.5}$) cocrystallized with Opx, which produced a penetrative texture into the large pyroxene crystals (Figs. 1 and 7). It is unclear whether these intergrowths were formed after incorporation of the Opx crystals into the 15434 parent magma (some groundmass plagioclase has ($An_{>92.5}$) or formed in an unrelated magma). Plagioclase with $An_{<92.5}$ is found within the groundmass and also intergrown with pigeonite–augite overgrowths on the large Opx crystals and is interpreted to have formed post eruption as the lava cooled on the lunar surface (Fig. 7). This detailed petrographic and mineralogical study of 15434,181 demonstrates the intricacies of understanding endogenous KREEP basalt petrogenesis. It also demonstrates that magmas existed within the Moon that contained incompatible trace element abundances above those that are typically present in KREEP basalts from the existing sample collection.

ACKNOWLEDGMENTS

We thank Paul Carpenter at Washington University in St. Louis for help and instruction on using the electron microprobe. We thank Tony Simonetti for all the help provided while using the LA-ICP-MS at Notre Dame (and for teaching the ICP-MS class). We also thank the reviewers for their patience. This work was supported by NASA Grant NNX11AH48G from the LASER program to Dr. Clive Neal.
Editorial Handling—Dr. Randy Korotev

REFERENCES

Anders E. and Grevesse N. 1989. Abundances of the elements: Meteoritic and solar. *Geochimica et Cosmochimica Acta* 53:197–214.

Bédard J. H. 2006. A catalytic delamination-driven model for coupled genesis of Archaean crust and sub-continental lithospheric mantle. *Geochimica et Cosmochimica Acta* 70:1188–1214.

Bindeman I. N., Davis A. M., and Drake M. J. 1998. Ion microprobe study of plagioclase-basalt partition experiments at natural concentration levels of trace elements. *Geochimica et Cosmochimica Acta* 62:1175–1193.

Blundy J. and Wood B. 1991. Crystal-chemical controls on the partitioning of Sr and Ba between plagioclase feldspar, silicate melts, and hydrothermal solutions. *Geochimica et Cosmochimica Acta* 55:193–209.

Blundy J. and Wood B. 1994. Prediction of crystal–melt partition coefficients from elastic moduli. *Nature* 372:452–454.

Church S. E., Bansal B. M., and Wiesmann H. 1972. The distribution of K, Ti, Zr, and Hf in Apollo 14 and 15 materials. In *The Apollo 15 lunar samples*, edited by Chamberlain J. and Watkins C. Houston, Texas: The Lunar Science Institute. pp. 210–213.

Cronberger K. and Neal C. R. 2013. KREEP basalts: Integrating quantitative textural analysis with chemical data (abstract #3051). 44th Lunar and Planetary Science Conference. CD-ROM.

Cronberger K. and Neal C. R. 2014a. Apollo 14 KREEP-rich lithologies: Evidence for magma chamber processes (abstract #2394). 45th Lunar and Planetary Science Conference. CD-ROM.

Cronberger K. and Neal C. R. 2014b. Apollo 15 KREEP basalts: An integrated approach to determining origin and evolution (abstract #1622). 45th Lunar and Planetary Science Conference. CD-ROM.

Dickinson J. E. and Hess P. C. 1982. Zircon saturation in lunar basalts and granites. *Earth and Planetary Science Letters* 57:336–344.

Dowty E., Keil K., Prinz M., Gros J., and Takahashi H. 1976. Meteorite-free Apollo 15 crystalline KREEP. Proceedings, 7th Lunar Science Conference. pp. 1833–1844.

Elardo S. M., Draper D. S., and Shearer C. K. 2011. Lunar magma ocean crystallization revisited: Bulk composition, early cumulate mineralogy, and the source regions of the highlands Mg-suite. *Geochimica et Cosmochimica Acta* 75:3024–3045.

Elkins-Tanton L. T., Van Orman J. A., Hager B. H., and Grove T. L. 2002. Re-examination of the lunar magma ocean cumulate overturn hypothesis: Melting or mixing is required. *Earth and Planetary Science Letters* 196:239–249.

Elkins-Tanton L. T., Burgess S., and Yin Q.-Z. 2011. The lunar magma ocean: Reconciling the solidification process with lunar petrology and geochronology. *Earth and Planetary Science Letters* 304:326–336.

Grove T. L. and Walker D. 1977. Cooling histories of Apollo 15 quartz-normative basalts. Proceedings, 8th Lunar Science Conference. pp. 1501–1520.

Hui H., Oshrin J. G., and Neal C. R. 2011. Investigation into the petrogenesis of Apollo 14 high-alumina basaltic melts through crystal stratigraphy. *Geochimica et Cosmochimica Acta* 75:6439–6460.

Irving A. J. 1975. Chemical, mineralogical, and textural systematics of non-mare melt rocks: Implications for lunar impact and volcanic processes. Proceedings, 6th Lunar Science Conference. pp. 363–394.

Irving A. J. 1977. Chemical variation and fractionation of KREEP basalt magmas. Proceedings, 8th Lunar Science Conference. pp. 2433–2448.

Irving A. J. and Frey F. A. 1984. Trace element abundances in megacrysts and their host basalts: Constraints on partition coefficients and megacryst genesis. *Geochimica et Cosmochimica Acta* 48:1201–1221.

Jolliff B. L., Haskin L. A., Colson R. O., and Wadhwa M. 1993. Partitioning in REE-saturating minerals: Theory, experiment, and modelling of whitlockite, apatite, and evolution of lunar residual magmas. *Geochimica et Cosmochimica Acta* 57:4069–4094.

Lunar Receiving Laboratory. 1971. *Lunar sample information catalog—Apollo 15*, Houston, Texas: NASA Manned Spacecraft Center. MSC 03209. 303 pp.

Marsh B. D. 1988. Crystal capture, sorting, and retention in convecting magma. *Geological Society of America Bulletin* 100:1720–1737.

Marsh B. D. 1996. Solidification fronts and magmatic evolution. *Mineralogical Magazine* 60:5–40.

Marsh B. D. 1998. On the interpretation of crystal size distributions in magmatic systems. *Journal of Petrology* 39:553–599.

Marsh B. D. 2013. On some fundamentals of igneous petrology. *Contributions to Mineralogy and Petrology* 166:665–690.

McKay G. A., Wiesmann H., Nyquist L. E., Wooden J. L., and Bansal B. M. 1978. Petrology, chemistry, and chronology of 14078: Chemical constraints on the origin of KREEP. Proceedings, 9th Lunar and Planetary Science Conference. pp. 661–687.

McKay G. A., Wiesmann H., Bansal B. M., and Shih C.-Y. 1979. Petrology, chemistry, and chronology of Apollo 14 KREEP basalts. Proceedings, 10th Lunar and Planetary Science Conference. pp. 181–205.

McKay G., Wagstaff J., and Yang S. R. 1986. Zirconium, hafnium, and rare earth element partition coefficients for ilmenite and other minerals in high-Ti lunar mare basalts: An experimental study. *Journal of Geophysical Research* 91:D229–D237.

Meyer C. and Hubbard N. J. 1970. High-potassium, high phosphorous glass as an important rock type in the Apollo 12 soil samples (abstract). *Meteoritics* 5:210–211.

Meyer C., Brett R., Hubbard N. J., Morrison D. A., McKay D. S., Aitken F. K., Takeda H., and Schonfeld E. 1971. Mineralogy, chemistry, and origin of the KREEP component in soil samples from the Ocean of Storms. Proceedings, 2nd Lunar Science Conference. pp. 393–411.

Nakamura Y., Fujimaki H., Nakamura N., Tatsumoto M., McKay G. A., and Wagstaff J. 1986. Hf, Zr, and REE partition coefficients between ilmenite and liquid: Implications for lunar petrogenesis. Proceedings, 16th Lunar and Planetary Science Conference, *Journal of Geophysical Research* 91: D239–D250.

Neal C. R. 2001. Interior of the Moon: The presence of garnet in the primitive deep lunar mantle. *Journal of Geophysical Research* 106:27865–27885.

Neal C. R. and Kramer G. Y. 2003. The composition of KREEP: A detailed study of KREEP basalt 15386 (abstract #2023). 34th Lunar and Planetary Science Conference. CD-ROM.

Neal C. R. and Kramer G. Y. 2006. The petrogenesis of Apollo 14 high-Al basalts. *American Mineralogist* 91:1521–1535.

Neal C. R., Donohue P. H., Fagan A. L., O'Sullivan K. M., Oshrin J., and Hui H. 2015. Distinguishing between pristine mare basalts and lunar impact melts: A non-destructive method using quantitative petrography. *Geochimica et Cosmochimica Acta* 148:62–80.

Nemchin A. A., Pidgeon R. T., Whitehous M. J., Vaughan J. P., and Meyer C. 2008. SIMS U-Pb study of zircon from Apollo 14 and 17 breccias: Implications for the evolution of lunar KREEP. *Geochimica et Cosmochimica Acta* 72:668–689.

Pearce N. J. G., Perkins W. T., Westgate J. A., Gorton M. P., Jackson S. E., Neal C. R., and Chenery S. P. 1997. A compilation of new and published major and trace element data for NIST SRM 610 and NIST SRM 612 glass reference materials. *Journal of Geostandards and Geoanalysis* 21:115–144.

Putirka K. D. 2008. Thermometers and barometers for volcanic systems. *Reviews in Mineralogy and Geochemistry* 69: 61–120.

Rutherford M. J., Tonks B., and Holmberg B. 1996. Experimental study of KREEP basalt evolution: The origin of QMD and granite at the base of the lunar crust (abstract #1113). 27th Lunar and Planetary Science Conference. CD-ROM.

Ryder G. 1987. Petrographic evidence for nonlinear cooling rates and a volcanic origin for Apollo 15 KREEP basalts. *Journal of Geophysical Research* 92:E331–E339.

Ryder G. 1988. Quenching and disruption of lunar KREEP lava flows by impacts. *Nature* 336:751–754.

Ryder G. and Bower J. F. 1976. Poikilitic KREEP impact melts in the Apollo 14 white rocks. Proceedings, 7th Lunar Science Conference. *Solar System Exploration Division Planetary Science Branch Publication* 81 (JSC #24035). 222 pp.

Ryder G. and Sherman S. B. 1989. The Apollo 15 coarse fines (4–10 mm). *Solar System Exploration Division Planetary Science Branch Publication* 81 (JSC #24035). pp. 1925–1948.

Salpas P. A., Taylor L. A., and Lindstrom M. M. 1987. Apollo 17 KREEPy basalts: Evidence for nonuniformity of KREEP. Proceedings, 17th Lunar and Planetary Science Conference. *Journal of Geophysical Research* 92: E340–E348.

Schneider C. A., Rasband W. S., and Eliceiri K. W. 2012. NIH Image to ImageJ: 25 years of image analysis. *Nature Methods* 9:671–675.

Shih C.-Y. 1977. Origins of KREEP basalts. Proceedings, 8th Lunar and Planetary Science Conference. pp. 2375–2401.

Simon S. B., Papike J. J., and Laul J. C. 1988. Chemistry and petrology of the Apennine Front, Apollo 15, Part I: KREEP basalts and plutonic rocks. Proceedings, 18th Lunar and Planetary Science Conference. pp. 187–201.

Snyder G. A., Taylor L. A., and Neal C. R. 1992. A chemical model for generating the sources of mare basalts:

Combined equilibrium and fractional crystallization of the lunar magmasphere. *Geochimica et Cosmochimica Acta* 56:3809–3823.

Spera F. J. 1992. Lunar magma transport phenomena. *Geochimica et Cosmochimica Acta* 56:2253–2265.

Sun C. and Liang Y. 2013. Distribution of REE and HFSE between low-Ca pyroxene and lunar picritic melts around multiple-saturation points. *Geochimica et Cosmochimica Acta* 119:340–358.

Taylor S. R. 1982. *Planetary science: A lunar perspective*. Houston, Texas: Lunar and Planetary Institute. 481 p.

Taylor G. J., Martel L., and Spudis P. D. 2012. The Hadley-Apennine KREEP basalt igneous province. *Meteoritics & Planetary Science* 47:861–879.

Tepley F. J., Lundstrom C. C., McDonough W. F., and Thompson A. 2010. Trace element partitioning between high-An plagioclase and basaltic to basaltic andesite melt at 1 atmosphere pressure. *Lithos* 118:82–94.

Vaniman D. T. and Papike J. J. 1980. Lunar highland melt rocks: Chemistry, petrology and silicate mineralogy. *Proceedings of the Conference on the Lunar Highlands Crust*, edited by Papike J. J. and Merrill R. B. New York: Pergamon. pp. 271–337.

Warren P. H. 1985. The magma ocean concept and lunar evolution. *Annual Review of Earth and Planetary Sciences* 13:201–240.

Warren P. H. 1988. The origin of pristine KREEP—Effects of mixing between UrKREEP and the magmas parental to the Mg-rich cumulates. Proceedings, 18th Lunar and Planetary Science Conference. pp. 233–241.

Warren P. H. 1989. KREEP: major-element diversity, trace-element uniformity (almost). In *Moon in Transition: Apollo 14, KREEP, and Evolved Lunar Rocks, LPI Technical Report* 89-03. pp. 149–153.

Warren P. H. 1993. A concise compilation of petrologic information on possibly pristine nonmare Moon rocks. *American Mineralogist* 78:360–376.

Warren P. H. and Wasson J. T. 1977. Pristine nonmare rocks and the nature of the lunar crust. Proceedings, 8th Lunar Science Conference. pp. 2215–2235.

Warren P. H. and Wasson J. T. 1978. Compositional-petrographic investigation of pristine non-mare rocks. Proceedings, 9th Lunar and Planetary Science Conference. pp. 185–217.

Warren P. H. and Wasson J. T. 1979. The origin of KREEP. *Reviews of Geophysics and Space Physics* 17:73–88.

Warren P. H., Afiattalab F., and Wasson J. T. 1978. Investigation of unusual KREEPy samples—Pristine rock 15386, cone crater soil fragments 14143, and 12023, a typical Apollo 12 soil. Proceedings, 9th Lunar and Planetary Science Conference. pp. 653–660.

Warren P. H., Taylor G. J., Keil K., Kallemeyn G. W., Shirley D. N., and Wasson J. T. 1983. Seventh foray: Whitlockite-rich lithologies, a diopside-bearing troctolite, ferroan anorthosites and KREEP. Proceedings, 14th Lunar and Planetary Science Conference, *Journal of Geophysical Research* 88:B151–B164.

Wieczorek M. A., Zuber M. T., and Phillips R. J. 2001. The role of magma buoyancy on the eruption of lunar basalts. *Earth and Planetary Science Letters* 185:71–80.

Wood B. J. and Blundy J. D. 2001. The effect of cation charge on crystal-melt partitioning of trace elements. *Earth and Planetary Science Letters* 188:59–71.

Wright T. L. and Fiske R. S. 1971. Origin of the differentiated and hybrid lavas of Kilauea volcano, Hawaii. *Journal of Petrology* 12:1–65.

Yao L., Sun C., and Liang Y. 2012. A parameterized model for REE distribution between low-Ca pyroxene and basaltic melts with applications to REE partitioning in low-Ca pyroxene along a mantle adiabat and during pyroxenite-derived melt and peridotite interaction. *Contributions to Mineralogy and Petrology* 164:261–280.